PCCP

Evaluation of Electrochemical Properties of Nanostructured Metal Oxide Electrodes Immersed in Redox-Inactive Organic Media

Journal:	*Physical Chemistry Chemical Physics*
Manuscript ID	CP-ART-05-2021-002370.R1
Article Type:	Paper
Date Submitted by the Author:	27-Jul-2021
Complete List of Authors:	Brewster, David; University of Rochester, Chemistry Koch, Melissa; University of Rochester, Chemistry Knowles, Kathryn; University of Rochester, Chemistry

Evaluation of Electrochemical Properties of Nanostructured Metal Oxide Electrodes Immersed in Redox-Inactive Organic Media

David A. Brewster,[a] Melissa D. Koch,[a] Kathryn E. Knowles[*]

Department of Chemistry, University of Rochester, Rochester, NY 14627

[*]e-mail: kknowles@ur.rochester.edu

ABSTRACT

This paper describes analysis of dropcast nanocrystalline and electrochemically deposited films of NiO and α-Fe_2O_3 as model metal oxide semiconductors immersed in redox-inactive organic electrolyte solutions using electrochemical impedance spectroscopy (EIS). Although the data reported here fit a circuit commonly used to model EIS data of metal oxide electrodes, which comprises an RC circuit nested inside a second RC circuit that is in series with a resistor, our interpretation of the physical meaning of these circuit elements differs from that applied to EIS measurements of metal oxide electrodes immersed in redox-active media. The data presented here are most consistent with an interpretation in which the nested RC circuit represents charge transfer between the metal oxide film and the underlying metal electrode, and the non-nested RC circuit represents the resistance and capacitance associated with formation of a charge-compensating double-layer at the exposed interface between the metal electrode and electrolyte solution. Applying this interpretation to analysis of EIS data collected for metal oxide films in organic media enables the impact of film morphology on electrochemical behavior to be distinguished from the effects of the intrinsic electronic structure of the metal oxide. This distinction is crucial to the evaluation of nanostructured metal oxide electrodes for electrochemical energy storage and electrocatalysis applications.

INTRODUCTION

Transitioning to an economy that depends exclusively on renewable sources of energy requires new systems for energy storage, such as electrochemical energy storage *via* batteries and chemical energy storage *via* photocatalytic generation of fuels,[1] and electrification of chemical manufacturing industries.[2] Importantly, these technologies must be based on sustainable and scalable materials in order to be viable for achieving this transition. Metal oxide semiconductors are a promising class of electrode materials for electrochemical and photocatalytic applications;[3-8] however, optimizing their performance in energy storage and electrocatalysis technologies requires facile and reliable methods of *in situ* characterization. Electrochemical measurements offer an advantageous method of characterization in which electrode properties can be analyzed *in situ* under relevant working conditions, e.g. under ambient pressure and in the presence of electrolyte ions. Electrochemical impedance spectroscopy (EIS) in particular can distinguish Faradaic from non-Faradaic charge flow, discern specific interfaces within an electrode system (i.e. substrate/semiconductor, semiconductor/electrolyte, and semiconductor/semiconductor interfaces), and provide quantitative evaluation of the energetic positions of band-edge states and interactions between ions and electrodes at the semiconductor/electrolyte interface.[9-12] EIS measurements can reveal information about redox-shifting of band-edge potentials in response to doping or changes in pH as well as the permeability of an electrode with respect to intercalation of working ions.[3, 6] Knowledge of band-edge potentials is critical to the design of efficient photoelectrocatalytic systems and improved photovoltaic heterojunctions. EIS measurements can also reveal mid-gap states that cannot be accessed optically but still contribute to Fermi-level pinning.[6, 13]

Extracting physically meaningful and accurate information from EIS measurements relies on both the choice of equivalent circuit applied to fit EIS data and the physicochemical interpretation of the individual elements of which the equivalent circuit is composed.[10, 14] Although there is typically general agreement on the choice of equivalent circuit used to model specific types of electrochemical systems, there are often competing interpretations of the physical meaning of the individual circuit elements.[15] EIS data collected for metal oxide semiconductor films immersed in liquid electrolyte are typically fit with either a [R([R(RC)]C)] equivalent circuit, referred to as Circuit A, or a [R(RC)] equivalent circuit, referred to as Circuit B (Figure 1).[10] Circuit A contains three resistors in series, R_1, R_2, and R_3; in parallel to R_1 and R_2 are constant phase elements (CPEs)

denoted C_1 and C_2, respectively. Due to the complex electrostatic structure of a nanocrystalline semiconductor/liquid electrolyte junction, CPEs are typically used to describe both the capacitance associated with the nonuniform charge-compensating double-layer that forms at the semiconductor/electrolyte interface as well as the capacitance associated with charge transfer across an interface. The impedance of a CPE, Z_{CPE}, is given by equation 1,[11, 15, 16] where j is the

$$Z_{CPE} = \frac{1}{Q(j\omega)^N} \quad (1)$$

imaginary number, ω is the angular frequency of the sinusoidal applied voltage, and Q and N characterize the nonlinear capacitance. Q has units of $F \cdot s^{N-1}$ and N is a unitless parameter with a value between zero and one. When $N = 1$, Q has units of F; when $N \neq 1$, Q has units $s^N \cdot \Omega^{-1}$.[11] The value of N characterizes the nature of the frequency dependence in a CPE. As N approaches unity, Z_{CPE} behaves as an ideal parallel-plate capacitor; when N is equal to 0.5, Z_{CPE} is mathematically equivalent to a Warburg element representative of diffusion limited mass transfer; when N is equal to zero, Z_{CPE} is mathematically equivalent to that of a pure resistor.[11, 16] The fitted Q and N values can be used to calculate an effective capacitance, C_{eff}, given by equation 2 where R is the resistance in parallel with the CPE (i.e. R_2 with C_2).[11, 16] All capacitance values reported in this work correspond to the effective capacitance of a CPE and are calculated using equation 2.

$$C_{eff} = \left[QR^{(1-N)}\right]^{1/N} \quad (2)$$

Circuit B is distinguished from Circuit A by loss of the nested R_1 and C_1 circuit elements. Figure 1 contains representative Bode and Nyquist plots that correspond to Circuit A and Circuit B. Each RC component in an equivalent circuit corresponds to a semicircle in a Nyquist plot and a peak in a Bode plot.[11, 17] Nyquist and Bode plots describing Circuit B each contain a single feature. Since Circuit A contains a second RC component in series with R_2, it produces a Nyquist plot comprised of two semicircles, which often overlap in frequency to resemble a semi-ellipsoid, and a Bode plot containing two peaks. These two features can be resolved when the values of C_1 and C_2 are similar in magnitude or when $R_1 >> R_2$, but they become indistinguishable from each other in the limits where $C_1 >> C_2$ or $C_2 >> C_1$, or when $R_1 << R_2$ (See Supporting Information, Figure S1).[10] In these limits, the EIS data can be fit adequately to circuit B.

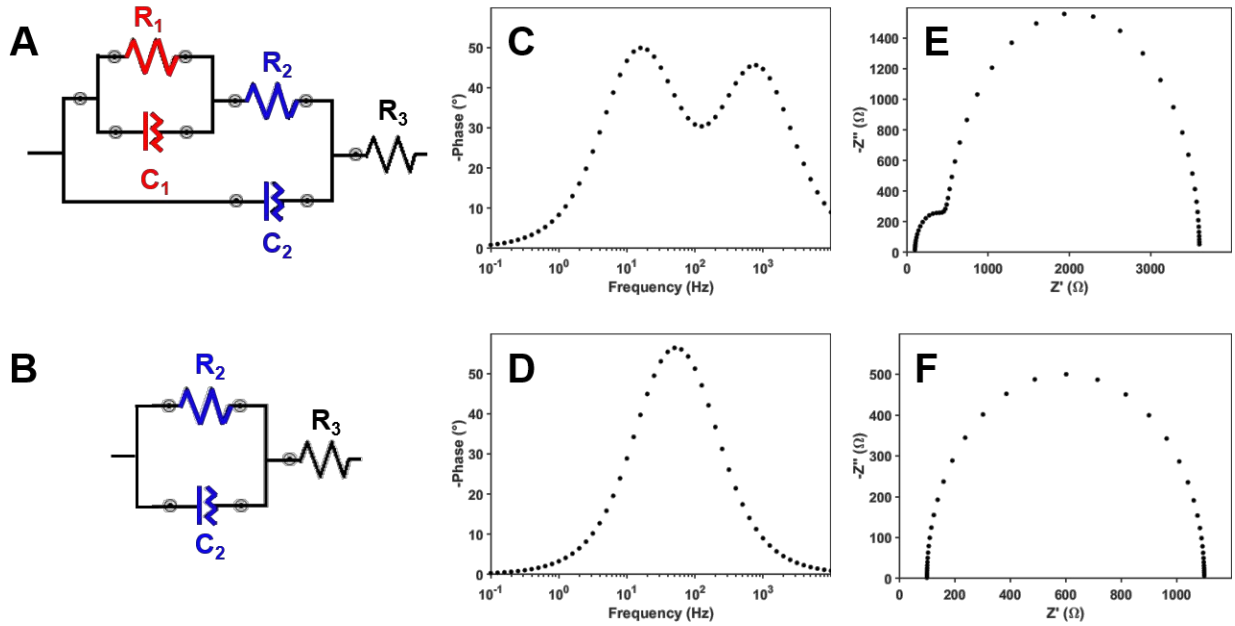

Figure 1. A) Equivalent Circuit A. Bode and Nyquist plots corresponding to Circuit A are shown in (**C**) and (**E**), respectively. **B**) Equivalent Circuit B. Bode and Nyquist plots corresponding to Circuit B are shown in (**D**) and (**F**), respectively.

When a porous thin-film metal oxide electrode is immersed in a liquid electrolyte, three types of interfaces are produced: (i) the interface between the conductive substrate and metal oxide semiconductor, (ii) the semiconductor/electrolyte interface, and (iii) the interface formed between the underlying conductive substrate and the liquid electrolyte that has percolated through the pores of the metal oxide film. The relative magnitudes of the resistances and capacitances characterizing charge flow across these interfaces, which are modeled by equivalent circuits such as those shown in Figure 1, depend on the properties of *both* the semiconductor and the electrolyte. For example, aqueous solutions do not behave as innocent media when measuring the electrochemical response of a metal oxide film. Metal oxide surfaces are readily hydrolyzed in the presence of water and easily corroded at low pH.[18-20] Furthermore, the measured flat band potential of a metal oxide in water is expected to (but does not always) exhibit a Nernstian dependence on pH.[21] Density functional theory calculations indicate that the presence of water can cause a significant shift in the energetic positions of valence and conduction band states of a metal oxide semiconductor.[22] Consequently, the semiconductor/electrolyte interface dominates the impedance response of metal oxide films immersed in aqueous media. EIS data collected for metal oxide electrodes in aqueous electrolytes are often fit with circuit A where R_2 and C_2 are assigned to resistive and capacitive

properties of the bulk film and R_1 and C_1 represent surface states.[5, 6, 23-25] Additionally, electrochemical measurements carried out in water are limited by the relatively small voltage window over which water is stable - the difference between the reduction and oxidation potentials of water is only 1.23 V. In contrast, nonaqueous solvents, such as acetonitrile, are stable over a much larger voltage window (typically 3-4 V) and exhibit very weak or nonexistent chemical interactions with metal oxide surfaces.[26] Characterizing the electrochemical behavior of metal oxide films in nonaqueous electrolytes is important for the development and understanding of electrocatalytic and photoelectrocatalytic organic transformations for which metal oxide semiconductors are an important emerging class of catalyst.[27]

Herein we report a systematic investigation of the application of circuit A to fit EIS data collected for prototypical NiO and α-Fe_2O_3 metal oxide electrodes immersed in redox-inert organic electrolytes. We examined films fabricated by both bulk electrochemical deposition and dropcasting from dispersions of colloidal nanocrystals in order to ascertain the impact of film morphology on its electrochemical response. Controlled variation of the ionic radii of the electrolyte and the physical pathway between the working and counter electrodes demonstrates explicitly that the first series resistance (R_3) is largely dependent on the average pathlength between the working and counter electrodes and independent of electrolyte size. Importantly, we demonstrate that EIS measurements of metal oxide semiconductor films in organic media enables simultaneous yet independent evaluation of (i) the absolute energetic positions of any electronic states in the metal oxide that are available for interfacial charge transfer, rather than only those that are catalytically active and (ii) the impacts of morphology on the overall electrochemical response of the metal oxide film. We find that the morphology of the metal oxide film and the ionic radii of the electrolytes impact the values of R_2 and C_2, whereas values for the nested components R_1 and C_1 exhibit minimal variation with electrode morphology and electrolyte size. We conclude that R_2 and C_2 are related to the porosity of the metal oxide film, and R_1 and C_1 describe charge transfer from the metal substrate into and through the metal oxide film.

EXPERIMENTAL METHODS

Electrochemical Deposition of Bulk Metal Oxide Films.

General Considerations. All electrochemical depositions were performed at room temperature with a standard three-electrode system in an undivided cell. The reference and counter electrodes

were Ag|AgCl (3M NaCl, Basi MF-2052) and a Pt mesh, respectively. Films were deposited on a working electrode of Au coated float glass (EMF, TA134). Prior to depositions, the working electrodes were cut into 25 x 25 mm squares and sonicated for 10 minutes each in hexane, Nanopure water, and isopropanol. For all depositions the working electrode was submerged to a depth of 15 mm in the deposition solution.

Deposition of NiO. Nickel (II) oxide films were prepared following the method reported by Rodzi, *et al*.[28] Nickel (III) oxyhydroxide (NiOOH) was deposited initially under potentiostatic conditions at a potential of 1.1 V vs. Ag|AgCl applied for 60 minutes to a Au electrode immersed in an electrolyte solution of 0.1 M nickel (II) sulfate (Oakwood Chemicals, 99%), 0.1 M sodium acetate (Baker Analyzed Reagent, ACS Grade), and 0.1 M sodium sulfate (EMSURE, ACS, ISO Grade). The film was subsequently calcined in air at 300 °C for one hour to form NiO.

Deposition of α-Fe_2O_3. We modified a method reported previously by Jiao, *et al.* for the electrochemical deposition of α-Fe_2O_3 thin films.[29] Goethite (α-FeOOH) was deposited onto the working electrode under potentiostatic conditions for 30 minutes with an applied potential of 0.697 V vs. Ag|AgCl in an electrolyte solution of 0.1 M ammonium iron (II) sulfate (Acros, 99%) and 0.4 M potassium acetate (Sigma, 99%). The film was subsequently calcined in air at 400 °C for one hour to produce α-Fe_2O_3. We note that applying the deposition potential for one hour instead of 30 minutes resulted in a substantially thicker film that produced an inductive loop in the Nyquist plot at high frequencies (see Supporting Information, Figure S2). This behavior is a consequence of the increased electrochemical time constant arising from the extra time required for the supporting electrolyte to sense the potential applied to the metal oxide film and form a charge-compensating double-layer.[9]

Once prepared, each NiO and α-Fe_2O_3 film was cut into two 25 x 10 mm rectangles for electrochemical analysis. The remaining 25 x 5 mm rectangle is reserved for further material characterization by powder X-ray diffraction (pXRD), X-ray photoelectron spectroscopy (XPS), and scanning electron microscopy (SEM, see Supporting Information Figures S3-S5).

A 6.5 x 5 mm electrochemical working area was defined by covering the designated area of the metal oxide film with a piece of Kapton tape and carefully covering the remainder of the film with a protective coating of polydimethylsiloxane (PDMS, Sylgard 184 Silicone Elastomer). The PDMS was cured for 45 minutes at 100 °C and the piece of Kapton, underneath the PDMS

protective layer, was removed with an X-ACTO blade to reveal the working area of the metal oxide electrode.

Synthesis of Metal Oxide Nanocrystals.

NiO. NiO nanocrystals were synthesized following our previously reported method.[30] Briefly, 1.11 mmol of nickel (II) decanoate decylamine complex $Ni(C_{10}H_{19}O_2)_2(C_{10}H_{23}N)_2$ is loaded into a 25 mL Teflon liner with 16 mL of *tert*-butanol, then sealed and reacted at 180 °C for 8 hours. Once cooled to room temperature, the reaction product was retrieved from the Teflon liner and purified with successive washing/centrifugation in ethanol, 1:1 v/v ethanol:hexane, and hexane to produce a green supernatant containing NiO nanocrystals.

α-Fe_2O_3. α-Fe_2O_3 nanocrystals were synthesized following our previously reported method.[31] Specifically, 1.11 mmol iron (III) laurate, 10.67 mL of water, 5.33 mL ethanol, and 3.33 mmol dodecylamine were loaded into a 25 mL Teflon liner. The Teflon liner was then sealed, placed in a stainless-steel autoclave, and heated at 180 °C for 8 hours. Once cooled to room temperature, the solid reaction product was retrieved from the Teflon liner and purified with successive washing/centrifugation from ethanol, 1:1 v/v ethanol:hexane, and hexane to produce a red precipitate comprising hematite nanocrystals.

All nanocrystal samples were characterized by p-XRD, XPS, and transmission electron microscopy (TEM, see Supporting Information, Figure S6). We fabricated nanocrystalline films in contact with both Pt and Au underlying electrodes for electrochemical analysis. Films in contact with Pt were fabricated by dropcasting colloidal dispersions of NiO or α-Fe_2O_3 nanocrystals in a 1:1 v/v mixture of hexanes:ethanol onto a Pt disc electrode (Basi, MF-2013). The thicknesses of the films were controlled using a piece of Kapton tape containing a circular hole matching the diameter of the Pt electrode (d = 1.6 mm). Films in contact with Au were fabricated by dropcasting colloidal dispersions of NiO or α-Fe_2O_3 or nanocrystals in a viscous ethylene glycol dispersion onto Au coated float glass (25 x 5 mm) that was partially coated with PDMS. Nanocrystalline films on Pt were dried at 125 °C for one hour; nanocrystalline films on Au were dried at 200 °C for 40 minutes.

Electrochemical Impedance Spectroscopy.

All non-aqueous electrochemical impedance measurements were collected under nitrogen atmosphere in a dry glovebox (UniLab MBraun) using a standard three-electrode system comprising a Pt wire counter electrode, a non-aqueous $Ag|Ag^+$ reference electrode (BioLogic RE-

7), and metal oxide working electrode. Glassware was oven dried at 125 ºC for a minimum of 4 hours and cooled in an evacuated antechamber prior to use in the glovebox. A Metrohm Autolab PGSTAT128N potentiostat equipped with an FRA32M module was connected to the sample cell using air-tight electrical feedthroughs mounted in the wall of the glovebox. Two electrolyte systems were employed during this study: 0.1 M tetrabutylammonium hexafluorophosphate ($TBAPF_6$) and 0.1 M tetramethylammonium hexafluorophosphate ($TMAPF_6$), both in acetonitrile that was deoxygenated and dried on a Glass Contour System (Pure Process Technology, LLC). $TBAPF_6$ was purified *via* recrystallization in hot ethanol three times and subsequently dried at 125 °C for two days. The purified product was stored under vacuum prior to use. EIS measurements were performed over the potential window -1.2 – 3 V vs. NHE (-1.75 -2.45 V vs. Ag/Ag^+). Cyclic voltammograms of a 1 mM solution of ferrocene ($E_{1/2}$ = 630 mV vs. NHE in acetonitrile)[32] were used to calibrate the $Ag|Ag^+$ reference electrode to NHE.

All EIS measurements were collected in 50 mV intervals, allowing ten seconds between measurements to equilibrate to each potential. A sinusoidal modulation with an amplitude of 25 mV was added to each applied potential, and the frequency of the modulation varied from 10,000 – 0.1 Hz. These conditions produced ellipsoidal Lissajous plots over the entire range of frequencies and potentials used for each metal oxide film (see Supporting Information, Figures S7 and S8).

RESULTS AND DISCUSSION

We performed EIS measurements on solution-processed nanostructured thin films of NiO and α-Fe_2O_3 fabricated by two different methods: electrochemical deposition from a solution of metal salt precursors and dropcast from a colloidal dispersion of pre-formed nanocrystals. Powder X-ray diffraction and X-ray photoelectron spectroscopy confirm the identity and phase-purity of the electrochemically deposited and dropcast NiO and α-Fe_2O_3 films (see Supporting Information, Figures S3 and S4). The morphologies of the films were characterized by scanning electron microscopy. The SEM images in Figure 2 reveal key differences among the morphologies of electrochemically deposited and dropcast nanocrystal films. For NiO, the electrochemically deposited NiO films comprise a porous network of NiO with a web-like appearance whereas the nanocrystal films exhibit large areas of empty space, either seen as cracks between areas of close-packed nanocrystals on platinum or significant distances between oblong platelets on gold. In contrast, the electrochemically deposited α-Fe_2O_3 films contain islands of α-Fe_2O_3 separated by

wide valleys whereas both nanocrystal samples form uniformly dense close-packed films. These morphologies are reproducible over large areas of the film (see Supporting Information, Figure S9).

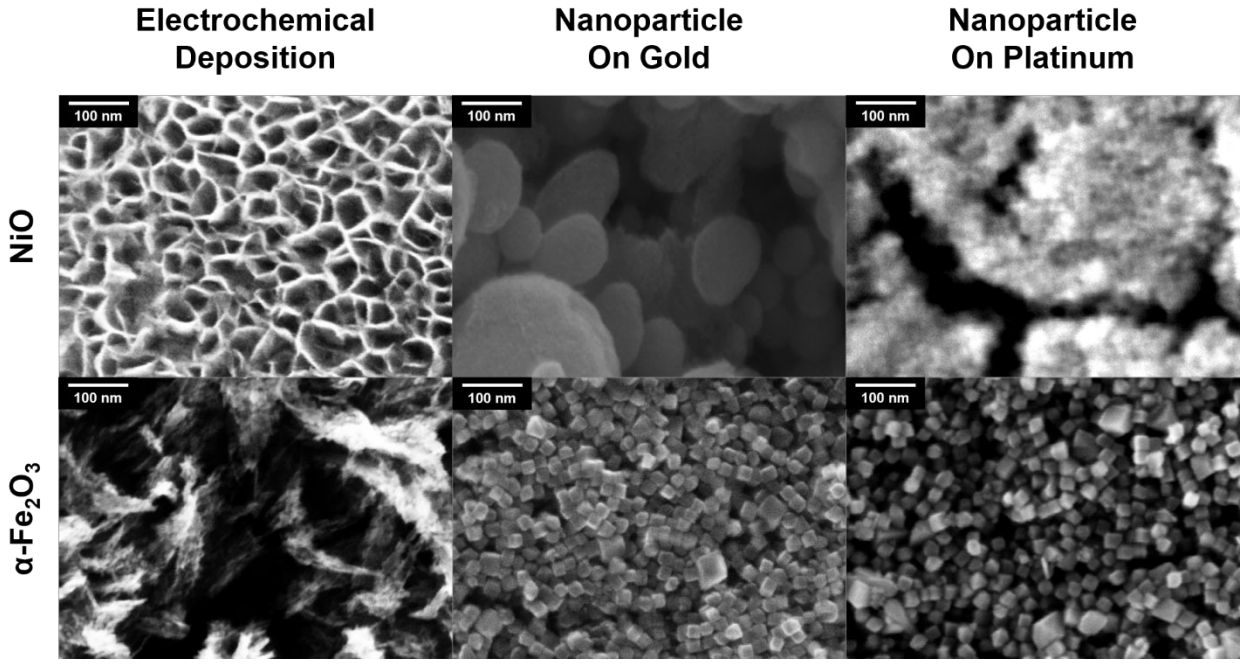

Figure 2. Representative SEM images of semiconductor electrodes, each with a scale bar of 100 nm. The electrochemically deposited NiO film (*top left*) shows a tightly packed structure with gaps limited to 10-40 nm in diameter The electrochemically deposited α-Fe_2O_3 film (*bottom left*) shows "leafy" structures with large (greater than 100 nm) gaps of empty space. The NiO nanocrystal sample on gold (*top middle*) shows that the >10 nm particles have packed into oblong platelets which leave large (greater than 100 nm) gaps of empty space in the film. The α-Fe_2O_3 nanocrystal sample on gold (*bottom middle*) shows semiconductor cubes with dimensions of ~20 nm with a tight packing that results in gaps no larger than 10-40 nm in diameter. The NiO nanocrystal sample on platinum (*top right*) does not show clear definition between nanocrystals, which are beyond the resolving capability of the instrument (d = 3.6 nm by TEM), but clearly indicates large cracks and gaps wider than 100 nm throughout the sample. The α-Fe_2O_3 nanocrystal sample on platinum (*bottom right*) shows similar morphology to the α-Fe_2O_3 nanocrystal sample on gold with tightly packed semiconductor cubes.

Circuit A provides a better fit to EIS data of NiO and α-Fe_2O_3 films than Circuit B.

We evaluated Bode plots constructed from EIS data collected for nanocrystalline and electrochemically deposited films of NiO and α-Fe_2O_3 to determine which equivalent circuit best describes these data. Representative fits of Bode plots to the model circuits are included in the

Supporting Information (Figures S10 and S11). Figure 3 shows plots of $^{1}/_{C_1^2}$ versus applied potential for electrochemically deposited and nanocrystalline electrodes on Au with inset Bode plots for selected applied potentials. The same plots for nanocrystalline electrodes on Pt are included in the Supporting Information, Figure S12. Although the separation between features in the Bode plots obtained for both NiO films and the nanocrystalline α-Fe_2O_3 film varies with applied potential, each plot contains two peaks that often overlap. Such features are best described by model Circuit A. We note that the lower frequency side of each Bode plot is more sensitive to applied potential than the higher frequency side (see Figure S13 in the Supporting Information for a direct comparison). This behavior is similar to the behavior of a set of simulated Bode plots generated from Circuit A by varying the values of the nested R_1 and C_1 components while keeping the values of the non-nested R_2 and C_2 components constant. The nested RC circuit elements therefore make a larger contribution to the phase angle observed at lower frequencies whereas the phase angle observed at higher frequencies arises primarily from the non-nested RC circuit elements. In contrast, the electrochemically deposited α-Fe_2O_3 film produces Bode plots that exhibit two distinct features only for applied potentials that are more positive than +1 V versus NHE. For potentials that are more negative than +1 V versus NHE, the Bode plots for the electrochemically deposited α-Fe_2O_3 film exhibit only one peak or part of one peak and are therefore better described by model Circuit B. Overall, we conclude that circuit A provides the best description of most of our EIS data.

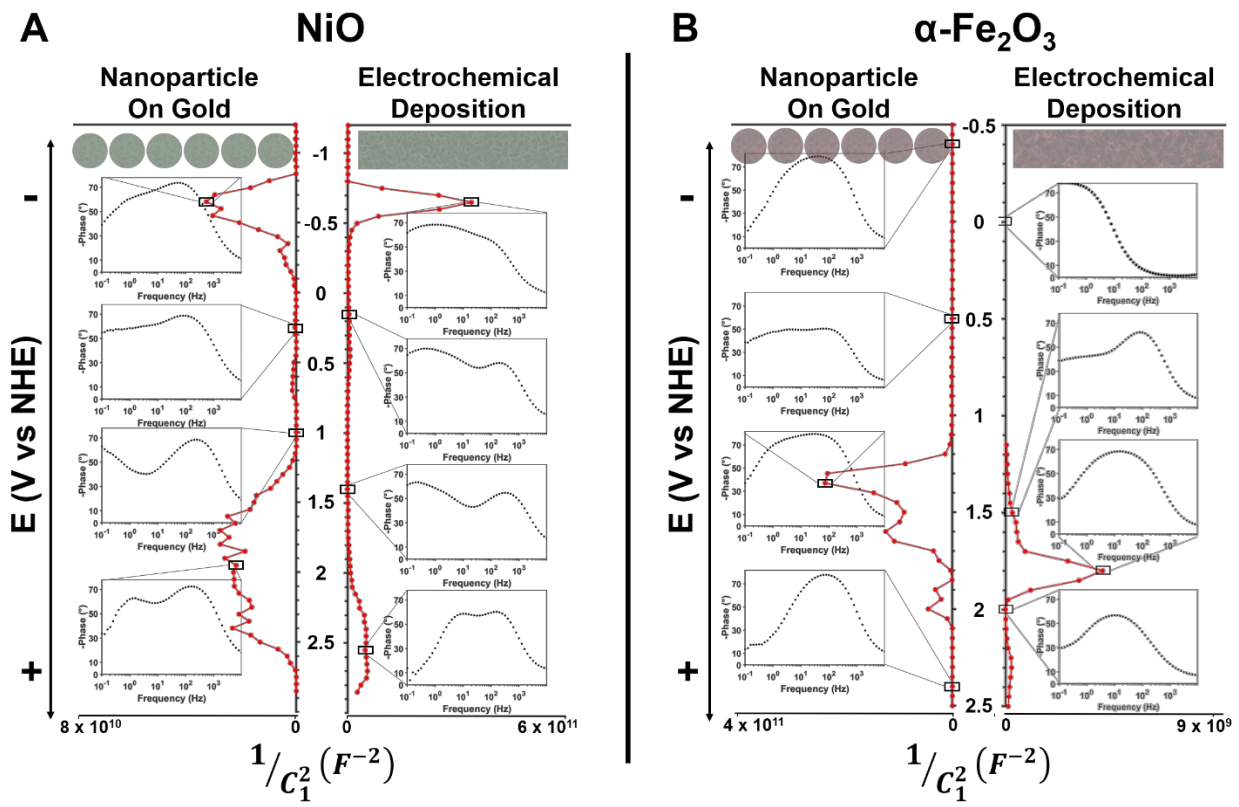

Figure 3. Representative plots of the inverse squared capacitance ($^{1}/_{C_1^2}$) versus applied potential for films of NiO (**A**) and α-Fe_2O_3 (**B**) comprised of nanoparticles dropcast on Au (*left*) or electrochemically deposited on Au (*right*). Points omitted from the plot of $^{1}/_{C_1^2}$ versus applied potential for the electrochemically deposited α-Fe_2O_3 film correspond to applied potentials for which Circuit B provided a sufficient fit. The insets in both (**A**) and (**B**) contain images of Bode plots that correspond to the potentials indicated by black boxes. All data was obtained in the presence of 0.1 M $TBAPF_6$ dissolved in dry acetonitrile.

Circuit A presents two diverging pathways for current to traverse: (i) through the nested R_1/C_1 circuit and R_2, or (ii) through C_2. For the porous NiO and α-Fe_2O_3 films studied here, we propose that the path through R_1/C_1 represents charge transfer across the metal/semiconductor interface and the path through C_2 represents accumulation of charge at the interface between the exposed metal substrate and the liquid electrolyte. The following two sections present data consistent with this interpretation.

R_1 and C_1 correspond to charge injection from the metal electrode into the metal oxide film.

In this section, we present experimental data that support the assignment of C_1 to the capacitance of the interface between the metal oxide semiconductor and the underlying metal electrode, and R_1 to the resistance associated with charge transfer across this interface.

First, we consider the impact we expect the applied potential to have on the capacitance of the interface between the metal electrode and the metal oxide film. When the potential applied to the metal electrode lies at a point within the band gap of the semiconductor where the density of states is negligible, there are no pathways available for charges injected into the metal electrode at that potential to flow into the semiconductor. Instead, charge accumulates in the metal, which results in higher values of the capacitance of this interface and the resistance associated with charge transfer across the interface from the metal electrode into the semiconductor. Shifting the potential applied to the metal electrode to a point that coincides with a larger density of states, such as the conduction or valence band-edges or mid-gap states, enables the injected charge to access the density of states available in the semiconductor at these potentials. Rather than accumulate in the metal, charge flows across the metal/semiconductor interface, which results in a smaller value of capacitance. Figure 4 compares plots of $1/C_1^2$ versus applied potential collected for nanoparticle and electrochemically deposited NiO films on Au substrates to cyclic voltammograms collected for the same films. The potentials corresponding to local maxima in the plots of $1/C_1^2$ (and, by extension, local minima in C_1) coincide with the potentials at which current onsets are observed in the cyclic voltammograms. These maxima also coincide with decreases in R_1 as shown in Figure S14 in the Supporting Information. These observations are consistent with our assignment of C_1 and R_1 to the capacitance and resistance, respectively at the metal/metal oxide interface.

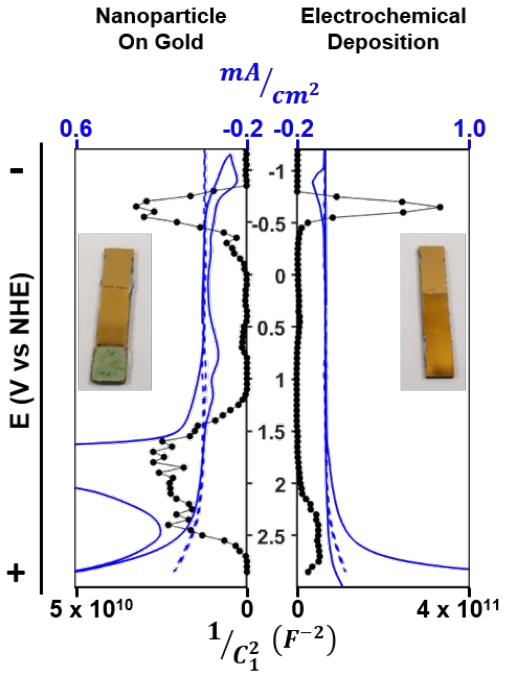

Figure 4. Plots of $^{1}/_{C_1^2}$ versus applied potential (black circles, bottom axes) and corresponding cyclic voltammograms (blue lines, top axes) obtained for a film of NiO nanocrystals dropcast on Au (*left*) and an electrochemically deposited film of NiO (*right*). Current density is reported with respect to the geometric surface areas of the metal oxide films and neglects roughness. The dashed blue lines represent cyclic voltammograms of bare Au electrodes. These data were measured in a 0.1 M solution of $TBAPF_6$ in acetonitrile. Inset: Photographic images of the respective NiO films.

Secondly, we observe that plots of $^{1}/_{C_1^2}$ versus applied potential for nanocrystalline and electrochemically deposited NiO films both show maxima at ~-0.7 and ~2.5 V vs. NHE (Figure 4). The separation of 3.2 V between these peaks is in good agreement with previously reported values of the band gap of NiO[30, 34, 35] and suggests that these peaks correspond to conduction and valence band states, respectively. The conduction and valence band positions of -0.7 and 2.5 V vs NHE for NiO are similar to values previously measured by Ozin and co-workers.[36] The positions of the conduction and valence bands of NiO relative to vacuum implied by these data are -3.7 and -7.0 eV, respectively, which are similar to the band-edge positions of NiO calculated from the absolute electronegativities of nickel and oxygen.[37]

We note that nanocrystalline NiO films on both gold and platinum exhibit multiple overlapping peaks in plots of $^{1}/_{C_1^2}$ versus applied potential that extend from ~1.5 - ~ 2.5 V vs. NHE (see Figure

5). We assign these features, which are not present in the electrochemically deposited NiO film, to surface states arising from nickel vacancies and/or interactions with decanoate or decylamine ligands remaining from nanoparticle synthesis. These states contribute to sub-bandgap features present in previously published UV-Vis spectra of these NiO particles[30] that are responsible for the observed green color of the dropcast nanoparticle (see insets to Figure 4). Notably, the electrochemically deposited film is colorless and does not contain these broad peaks in its plot of $1/C_1^2$ versus applied potential.

Previous reports of EIS measurements collected for NiO electrodes in redox-active aqueous or non-aqueous electrolytes (e.g. in the presence of surface-bound dye molecules and I^-/I_3^-) focus on a linear region in plots of $1/C^2$ versus applied potential that occurs between 0.4 and 0.8 V vs. NHE.[38-42] We observe local maxima in $1/C_1^2$ at similar potentials (see Supporting Information, Figure S15), however, the maximum value we measure for $1/C_1^2$ in this potential region is about two orders of magnitude smaller than that observed at -0.7 V and 2.5 V vs. NHE. Features observed between 0.4 and 0.8 V vs. NHE have been previously assigned to the flat-band potential of NiO,[38-42] however, the potentials where these features are observed coincide with the measured potential of $Ni^{2+/3+}$ redox events.[43] Furthermore, surface treatments demonstrated to impact the relative concentration of Ni^{2+} and Ni^{3+} on the surface of NiO films result in a shift in the potential at which this feature is observed.[42] Since our EIS measurements span a much larger potential window than previous reports, we are able to observe the large peaks in $1/C_1^2$ that arise from both the valence and conduction band-edges, and we therefore propose that the smaller peaks we observe at ~0.5 V vs. NHE arise from localized surface $Ni^{2+/3+}$ redox events.

In contrast to NiO films, plots of $1/C_1^2$ versus applied potential obtained for nanocrystalline and electrochemically deposited α-Fe_2O_3 films show a single feature (Figure 5). For α-Fe_2O_3 films dropcast from nanocrystal dispersions on Pt and Au, this peak appears at ~1.2 and ~1.4 V vs. NHE, respectively; for electrochemically deposited films, this peak appears at ~1.8 V vs. NHE. We hypothesize that this feature corresponds to a localized mid-gap state that provides the predominant pathway through which charges enter and leave the α-Fe_2O_3 films. Previous reports have also

identified localized mid-gap states as dominating charge flow into and out of α-Fe_2O_3 films and describe these states either as surface states[5, 24, 44] or electron small polarons.[45, 46] Importantly, this assignment implies that the conduction band and valence band states of α-Fe_2O_3 are, at best, minimally involved in interfacial charge transfer.

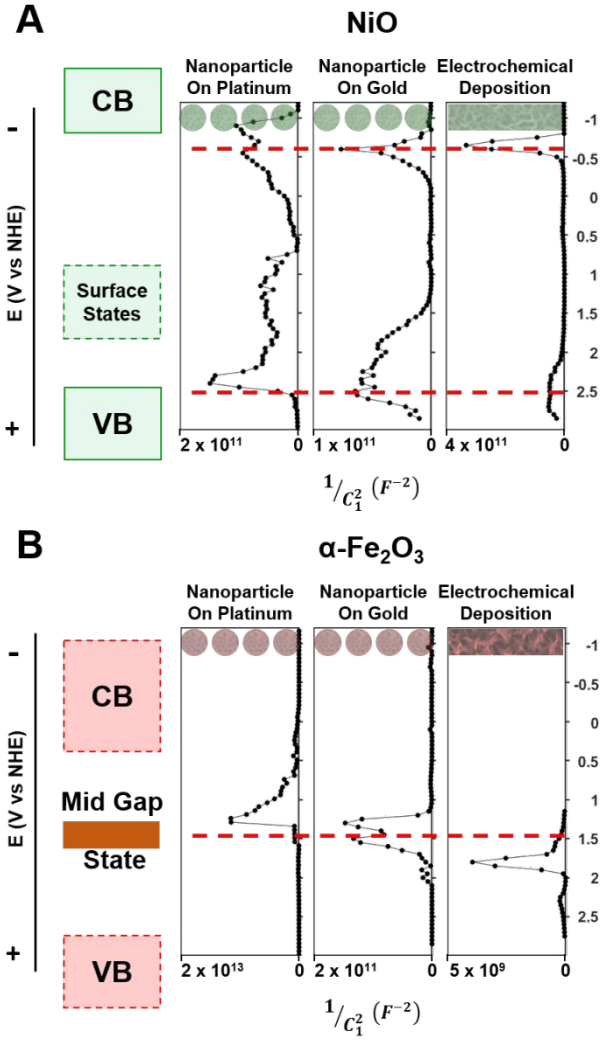

Figure 5. Plots of $^1/_{C_1^2}$ versus applied potential for nanoparticle on Pt (left-hand plots), nanoparticle on Au (middle plots) and electrochemically deposited (right-hand plots) films of NiO (**A**) and α-Fe_2O_3 (**B**). These data were averaged over three different films and measured in a 0.1 M solution of $TBAPF_6$ in acetonitrile. The red dashed lines are guides for the eye. The Supporting Information contains individual plots of each trial as well as plots of C_1 versus applied potential and representative cyclic voltammograms (Figures S16-S18). Local maxima in $^1/_{C_1^2}$ of NiO films correspond to valence (VB) and conduction (CB) band states, indicated with green rectangles on the far left of the figure. The peak observed in each α-Fe_2O_3 plot corresponds to a localized mid gap state, indicated as an orange rectangle on the far right of the figure.

We note that the plots of $1/C_1^2$ versus applied potential are highly non-linear for both the NiO and α-Fe_2O_3 films, and therefore cannot be described by the Mott-Schottky equation. This observation implies that the electronic structure of the metal/metal oxide interface in these films is not dominated by depletion-region behavior.[47] Consequently, the nanostructured NiO and α-Fe_2O_3 films used here effectively behave as intrinsic semiconductors with negligible carrier densities in the conduction and valence bands, rather than *p*- or *n*-type semiconductors. Herraiz-Cardona, et al. report similar observations for porous $CuGaO_2$ films.[48] Incorporation of magnesium dopants into these films increased the carrier density and resulted in linear Mott-Schottky plots. We suspect that the high surface-area to volume ratio that arises from the highly nanostructured morphology of the NiO and α-Fe_2O_3 films studied here enables defects, such as oxygen vacancies, to be compensated by localized surface charges rather than delocalized charges occupying valence or conduction band states.[49] Nevertheless, we find that plots of $1/C_1^2$ versus applied potential are still useful for analyzing EIS data because they highlight the local extrema that correspond to potentials where the densities of states available for current flow into the semiconductor are high.

Finally, the assignment of C_1 to the capacitance at the electrode/semiconductor interface implies that a Schottky barrier forms at this interface. The height of this Schottky barrier depends on the work function of the metal relative to the flat band potential of the semiconductor,[21] and should therefore change with the identity of the underlying metal electrode. This change in the Schottky barrier height should influence the potentials at which current begins to flow through the interface and, consequently, should result in a shift in the potentials at which peaks in the plots of $1/C_1^2$ appear. Figure 5 demonstrates that we observe a shift in the plot of $1/C_1^2$ versus applied potential for films of NiO and α-Fe_2O_3 nanoparticles dropcast onto a Au electrode compared to films of the same nanoparticles dropcast onto a Pt electrode (see Supporting Information, Figure S19 for superimposed data). These shifts of ~0.2 V are consistent with Schottky behavior at the metal/semiconductor interface and coincide with the difference between the open circuit potentials of bare Au and Pt electrodes measured *in situ* (0.6 V and 0.45 V vs. NHE, respectively). Overall,

the observation of shifts in the plots of $1/C_1^2$ versus applied potential are consistent with our assignment of C_1 to the capacitance of the metal/semiconductor interface.

C_2 describes the capacitance of the double-layer formed at the interface between the exposed metal electrode and the electrolyte solution.

The SEM images of the NiO films shown in Figure 2 demonstrate that the porosity of these films is large enough that it is reasonable to assume that the liquid electrolyte phase can access the underlying metal electrode and thus provide an alternate pathway for current that bypasses the semiconductor entirely. Importantly, since the acetonitrile electrolyte solution is not redox active, we expect the nature of this interface to be primarily capacitive. We therefore assign C_2 to this interface. If this assignment is valid, then the value of C_2 should depend on the size of the electrolyte ions relative to the surface area of exposed metal electrode, which depends on the porosity of the film. If the electrolyte ions are large relative to the surface area of exposed metal, then we expect to observe a smaller value of C_2 than we would observe for smaller electrolyte ions or a larger surface area of exposed metal.

In order to test this hypothesis, we performed EIS measurements on films of NiO with two different morphologies using two different electrolytes: tetramethylammonium hexafluorophosphate ($TMAPF_6$) and tetrabutylammonium hexafluorophosphate ($TBAPF_6$). $TMAPF_6$ and $TBAPF_6$ share a common anion, with an ionic radius of 0.234 nm, and have different cations with radii of 0.279 nm and 0.413 nm, respectively.[50, 51] Plots of $1/C_2^2$ versus applied potential obtained from EIS measurements of a film of NiO nanocrystals dropcast onto a Au electrode demonstrate no obvious dependence on electrolyte size; however, analogous plots of $1/C_2^2$ versus applied potential for an electrochemically deposited film of NiO on a Au electrode exhibit consistently smaller values of $1/C_2^2$ (i.e. larger values of C_2) for $TMAPF_6$ than $TBAPF_6$ (Figure 6). We note that the nanocrystalline film of NiO contains large gaps where the underlying metal electrode is exposed (see Figure 2), which diminish significantly the impact of the porous structure of the metal oxide film on the formation of a charge-compensating double layer at the interface between the exposed metal electrode and the electrolyte solution. The more tightly packed structure of the electrochemically deposited film is expected to exert a greater influence on

the formation of the double layer at the interface between the exposed metal electrode and the electrolyte and its measured capacitance. In contrast, plots of $^1/_{C_1^2}$ versus applied potential are largely independent of electrolyte size for both the nanocrystal and electrochemically deposited films (Figure 6).

In addition, we find that characterizing the metal/electrolyte interface directly through EIS measurements of bare Au or Pt electrodes yields values of $^1/_{C_2^2}$ that have a very similar dependence on applied potential as the values of $^1/_{C_2^2}$ values obtained from EIS measurements of metal oxide films on Au and Pt electrodes, respectively (see Figure S20 in Supporting Information). Based on these data, we propose that C_2 corresponds to the capacitance of the charge-compensating double layer formed by electrolyte ions at the metal/electrolyte interface that exists due to the porous nature of our metal oxide films. Previous EIS studies of porous $CuGaO_2$ films also assign a capacitive circuit element to the double-layer capacitance at the exposed interface between the electrolyte solution and the fluorine-doped tin oxide (FTO) substrate.[15, 48]

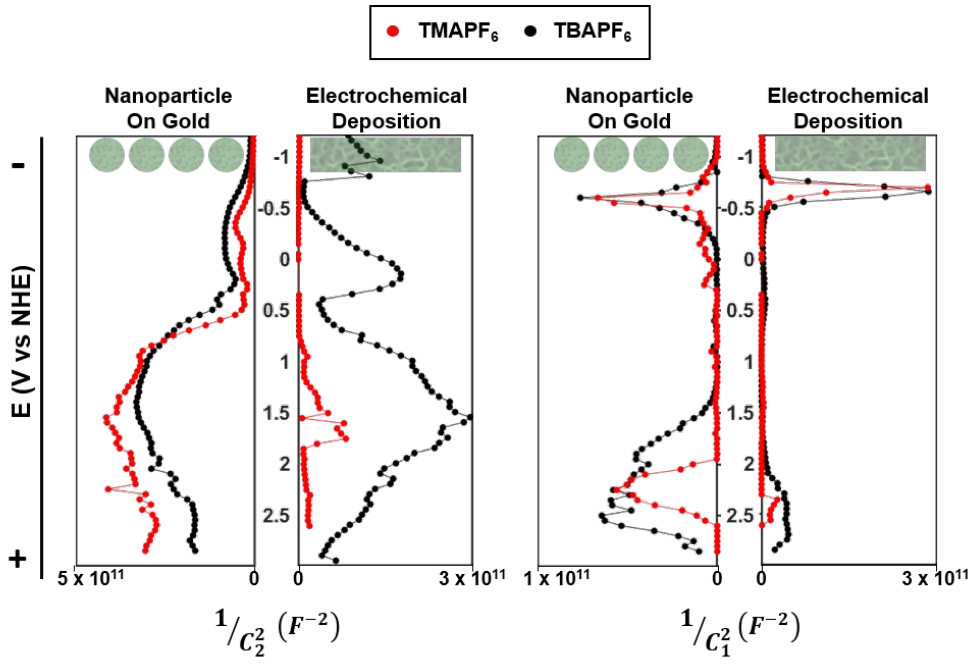

Figure 6. Representative plots of inverse squared capacitances ($^1/_{C_2^2}$ *left*, $^1/_{C_1^2}$ *right*) for nanoparticle electrodes of NiO on Au (green circles) compared to electrochemically deposited

electrodes of NiO (green rectangles), respectively. Data collected in 0.1 M $TMAPF_6$ correspond to red traces, while data collected in 0.1 M $TBAPF_6$ correspond to black traces.

The electrochemically active surface area of an electrode film is limited by the porous regions of the film that are accessible to electrolyte ions. For the metal oxide films examined here, this surface area includes both the porous metal oxide and any exposed area of the underlying metal electrode. The magnitude of the peak current observed in a cyclic voltammogram of a solution-phase analyte, as described by the Randles-Sevcik equation, is determined by several components such as: the electrochemically active surface area of the working electrode, the voltage scan rate, the diffusion coefficient and concentration of the analyte.[52] In the case of a porous electrode, inhibition of ion diffusion within the electrode pores leads to underestimation of the electrochemically active surface area when using the Randles-Sevcik equation, particularly at fast scan rates. This effect is visualized in cyclic voltammograms as a non-linear shift in both peak current and peak potential with changing scan rate.[53] Tabulating the electrochemically active surface area estimated by the Randles-Sevcik equation at various scan rates can therefore provide a qualitative assessment of the degree to which porosity impacts the behavior of an electrode. For example, applying the Randles-Sevcik equation to cyclic voltammograms of ferrocene collected using bare Au or Pt electrodes produces the same value for the electrode surface area over a broad range in scan rates (see Supporting Information Table S2 and Figure S21). In contrast, the electrochemically active surface area estimated by the Randles-Sevcik equation for the metal oxide films decreases monotonically with increasing scan rate, which indicates that the porosity of these films impacts their electrochemical response. This effect is more pronounced for the electrochemically deposited films than the nanocrystalline films. For example, the estimated electrochemically active surface area of the electrochemically deposited NiO film decreases by a factor of 4 as the scan rate increases from 0.025 to 0.5 V/s whereas the estimated electrochemically active surface area of the nanocrystalline NiO films on both Pt and Au only decreases by a factor of 1.5 over the same range in scan rate. Furthermore, when measured with the electrochemically deposited NiO film, the separation between the anodic and cathodic peaks of ferrocene doubles as the scan rate increases from 0.025 to 0.5 V/s, whereas this separation only increases by a factor of 1.2 for the nanocrystalline NiO films on Pt and Au. These observations imply that film porosity has a greater impact on the electrochemical behavior of the electrochemically deposited NiO film

than on the electrochemical behavior of the nanocrystalline NiO film on Au, which is consistent with the EIS data plotted in Figure 6.

R_2 describes the resistance associated with formation of a charge-compensating double layer at the electrode/electrolyte interface.

Figure S22 contains plots of the non-nested resistance R_2 versus applied potential obtained for nanostructured NiO films as well as the double-layer resistance measured for bare Au and Pt electrodes, and Table S3 compiles the average values of R_2 obtained for each of these films in $TMAPF_6$ and $TBAPF_6$. These data show that the average magnitude of R_2 obtained for films immersed in the larger $TBAPF_6$ electrolyte is larger than the average magnitude of R_2 obtained for films immersed in $TMAPF_6$. Furthermore, the average value of R_2 obtained for the electrochemically deposited NiO film is an order of magnitude smaller than the average values obtained for the nanocrystalline NiO film and bare electrodes. We assign R_2 to the resistance associated with formation of the charge-compensating double layer at the electrode/electrolyte interface. One factor that contributes to this resistance is the size of the electrolyte ions. Smaller electrolyte ions not only have larger diffusion coefficients but can also percolate more easily through porous electrodes and are therefore expected to produce lower values of double-layer resistance than larger electrolytes. Our observation of smaller values of R_2 for measurements conducted in the smaller $TMAPF_6$ electrolyte compared to the larger $TBAPF_6$ electrolyte is therefore consistent with our assignment of R_2 to the resistance associated with formation of the charge-compensating double-layer. Another factor that contributes to this double-layer resistance is the energy required to de-solvate the electrolyte ions. Higher energies of de-solvation contribute to larger double-layer resistances.[54, 55] For a film with small pore volumes, the electrolyte ions become de-solvated as they percolate through the film. Consequently, the contribution of de-solvation energy to the double-layer resistance decreases with decreasing pore size.[56, 57] This contrast implies that the tightly packed structure of the electrochemically deposited NiO film should result in a lower value of R_2 than the bare gold electrode and the gap-filled nanocrystalline NiO film, which is what we observe.

Solution resistance is the primary contributor to R_3.

The series resistance, R_3, has previously been reported to include the resistance associated with an ohmic contact between the metal oxide and underlying conductive substrate,[5, 6, 25] a solution resistance,[16, 58, 59] and other unspecified cell resistances,[23, 60] however the relative magnitudes of the contributions of each of these components to the series resistance is often unclear or not discussed. Here we present the results of experiments designed to probe explicitly the contribution of solution resistance to R_3. Figure 7 shows Nyquist plots obtained from electrochemical impedance analysis of Pt, Au, nanocrystalline α-Fe_2O_3 on Pt, electrochemically deposited α-Fe_2O_3 on Au, nanocrystalline NiO on Pt, and electrochemically deposited NiO on Au working electrodes in varying cell configurations and two different electrolyte solutions. These plots highlight the high frequency region near the origin (where φ is closest to 0°). In the high-frequency limit, the ability of the capacitive elements to store (and thereby impede) charge is minimal and the system exhibits primarily resistive behavior. The x-intercept in this region reflects the real resistance value of R_3 in ohms (Ω).[11, 14, 60] For Au, α-Fe_2O_3 @ Au, and NiO @ Au electrodes, the magnitude of R_3 does not depend strongly on the electrolyte or metal oxide, however, reorienting the working electrode with respect to the counter electrode results in a significant change in R_3 values that is consistent among all combinations of electrolyte and metal oxide systems. Facing the working electrode away from the counter electrode (system 2 configuration) causes a significant increase in R_3 values compared to those measured when the working electrode faces toward the counter electrode (system 1 configuration). We observe similar behavior for Pt, α-Fe_2O_3 @ Pt, and NiO @ Pt electrodes. Decreasing the distance between the bare Pt disc electrode and the bottom of the beaker, which increases the distance between the surface of the working electrode and the counter electrode, also causes a significant increase in the value of R_3 (see Supporting Information, Figure S23). Additionally, decreasing the concentration of electrolyte in the solution also increases the magnitude of R_3 (see Supporting Information, Figure S24 and Table S5), which is consistent with results observed in other studies that assign this resistor primarily to solution resistance.[61] These data indicate that the magnitude of R_3 depends strongly on the pathlength an electrolyte ion must travel between the working and counter electrodes and the concentration of electrolyte in solution. We therefore conclude that solution resistance comprises the primary contribution to R_3 for these systems.

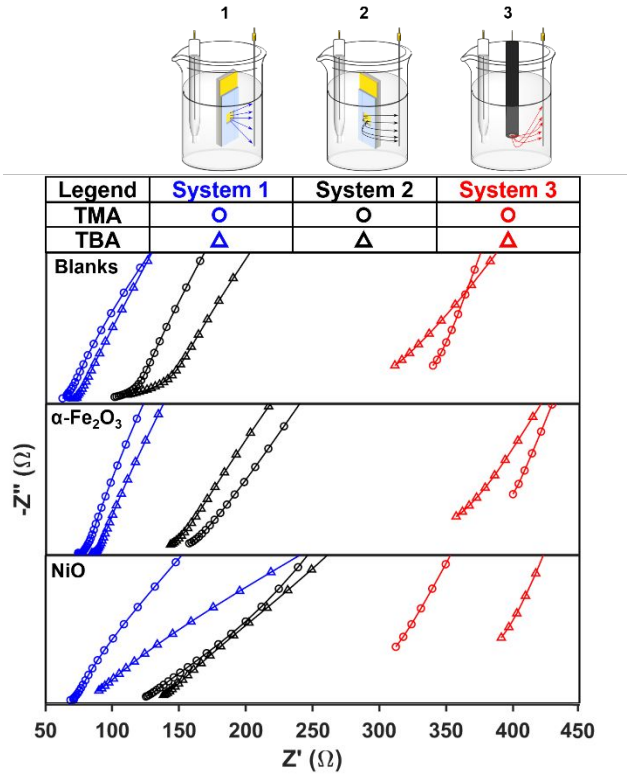

Figure 7. Nyquist plots for bare and oxide coated Au and Pt electrodes collected with three different electrode configurations. Each Nyquist plot has a y-axis that spans 0-300 Ω and an x-axis that spans 50-450 Ω. The x-intercept for each data series corresponds directly to the value of R_3. Blue traces represent data collected for bare (*top*), α-Fe_2O_3-coated (*middle*), and NiO-coated (*bottom*) Au electrodes positioned with the working electrode (film) facing the counter electrode (system 1 configuration); black traces represent bare (*top*), α-Fe_2O_3-coated (*middle*), and NiO-coated (*bottom*) Au electrodes positioned with the working electrode (film) facing away from the counter electrode (system 2 configuration); red traces represent bare (*top*), α-Fe_2O_3-coated (*middle*), and NiO-coated (*bottom*) Pt electrodes positioned with the working electrode (disk) perpendicular to the counter electrode (system 3 configuration). Circles represent data collected in a 0.1 M $TMAPF_6$/acetonitrile electrolyte solution and triangles represent data collected in a 0.1 M $TBAPF_6$/acetonitrile electrolyte solution. Although shifting between electrodes within a system does not have a consistent effect on the measured value of R_3, there is a clear shift in the measured R_3 values between systems 1-3 (see Supporting Information for tabulated values in Table S4). All trials are measured at 0 V versus an $Ag|Ag^+$ reference electrode (0.55 V vs. NHE).

Summary and Relationship to Previous Work.

Figure 8 summarizes our interpretation of EIS measurements obtained for solution-processed films of NiO and α-Fe_2O_3 in organic electrolytes and fit to Circuit A. Under applied negative bias, electrons flow from the metal substrate into the deposited oxide film. This charge transfer process is described by a resistance ($R_{CT} = R_1$), which parameterizes the kinetic barriers impeding electron flow into and through the metal oxide, and a capacitance ($C_{CT} = C_1$), which parameterizes the

density of states in the oxide available to accept electrons from the metal. The magnitudes of R_1 and C_1 therefore depend on the electronic structure of the metal oxide. The ability of the electrolyte cations (depicted as blue circles in Figure 8) to percolate into the film and form a charge compensating double layer at the surface of the electrode is determined by their ionic radii compared to the pore size of the oxide layer. The formation of this double layer is also described by two parameters: a resistance ($R_{DL} = R_2$), which parameterizes the energy required to organize the electrolyte ions into the double layer, and a capacitance ($C_{DL} = C_2$), which parameterizes the maximum number of cations the exposed metal surfaces can accommodate. Thus, the magnitudes of R_2 and C_2 depend on the morphology of the metal oxide film. Under a positive applied bias, electrons flow from the oxide into the metal electrode and the electrolyte anion compensates charge at the metal/electrolyte and semiconductor/electrolyte interfaces. The resistance associated with passing charge between the working and counter electrodes through the electrolyte solution to complete the circuit is primarily due to solution resistance and is described by $R_S = R_3$.

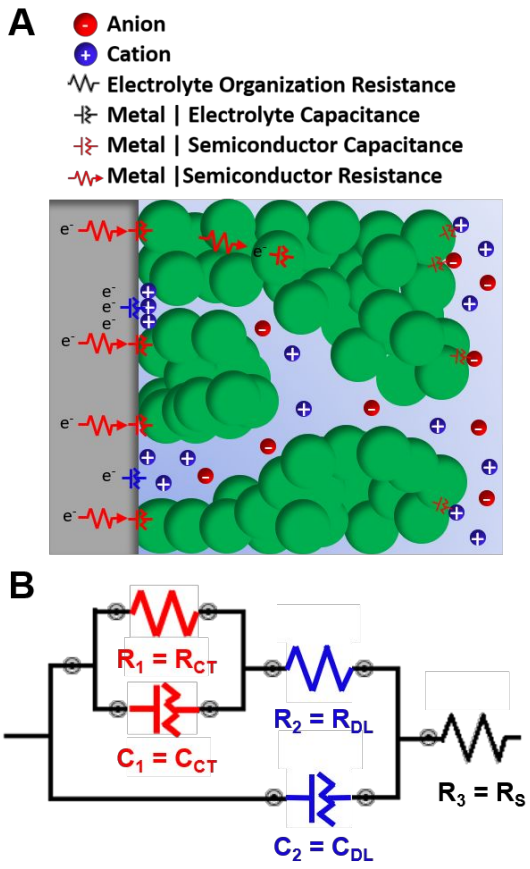

Figure 8. A) Cartoon illustration of a semiconductor electrode/electrolyte interface under a negative applied bias. The gray rectangle represents the metal substrate on which the semiconductor (green particles) is deposited and through which the potential is applied. **B**) Equivalent circuit describing the electronic behavior of the interface illustrated in part **A**. The charge transfer and double-layer resistances and capacitances are represented by equivalent circuit elements shown in red and blue, respectively. This circuit contains one additional circuit element ($R_S = R_3$), which is dominated by the solution resistance.

We note that we performed our EIS measurements in organic media over a range of applied potentials (-1.2 - 3 V vs. NHE) that were insufficient to reduce or oxidize the solvent (acetonitrile) or electrolyte ions (TBA^+, TMA^+, and PF_6^-). Rather, current flows across the semiconductor/electrolyte interface exclusively via the motion of supporting electrolyte ions. The charge transfer resistance at the semiconductor/electrolyte interface is therefore high compared to that at the metal/semiconductor interface. Furthermore, the surface area of the porous semiconductor/electrolyte interface is larger than the surface area of the metal/semiconductor interface, therefore we expect the capacitance of the semiconductor/electrolyte interface to be higher than that of the metal/semiconductor interface. Consequently, we considered a circuit in

which the metal/semiconductor and semiconductor/electrolyte interfaces are treated as two distinct pairs of parallel RC components that are in series with each other (Circuit C, see Supporting Information, Figures S25-S27). Modeling of the impedance response obtained from this circuit reveals that the two nested components are interchangeable. Additionally, depending on the relative magnitudes of the nested and non-nested resistances and capacitances, Circuit C produces an impedance response that is indistinguishable from that produced by Circuit A or Circuit B. Thus, even though Circuit C produces a more explicitly complete description of each type of interface present in our system, the impedance response we measure cannot resolve each of these components and we instead fit most of our data to Circuit A. Given our observation of the influence of the identity of the underlying metal electrode (Au or Pt) on the value of C_1 measured in a redox-inactive electrolyte, we conclude that the values of the nested circuit components measured under these conditions primarily reflect the behavior of the metal/semiconductor interface. EIS measurements of the same NiO electrodes performed in a redox-active electrolyte produce a significantly different response than was obtained in redox-inactive media (see Supporting Information, Figure S28). We interpret these observations to mean that, in the presence of a redox-active electrolyte, the semiconductor/electrolyte interface has a greater influence on the measured impedance response than in a redox-inactive electrolyte.

EIS measurements of metal oxide films in redox-inactive organic electrolytes offer three distinct advantages in the context of characterizing the performance of metal oxide electrodes in applications related to sustainable energy that do not involve photoelectrochemical water-splitting. (i) Organic electrolytes increase the useable electrochemical window from 1.23 V, which is the difference between the proton reduction and water oxidation potentials, to 3-4 V depending on the combination of solvent and supporting electrolyte.[62, 63] Access to a larger voltage window enables exploration of the entire band gap of metal oxide semiconductors with $E_g > 1.23$ V and is advantageous for battery applications.[64] (ii) Organic solvents are more suitable for exploring the use of metal oxide electrodes as electrocatalysts for various organic reactions whose reactants are not compatible with water. Examples include reduction, oxidation, hydroxylation, cycloaddition, dehydrogenation, and other important C-C bond forming reactions specifically catalyzed by metal oxides in organic media.[27] (iii) Rather than act as redox partners, redox inert electrolyte ions serve as probes of the porosity of the metal oxide film. This approach enables separation of the impact of the morphology of the electrode on its electrochemical behavior from the contributions of the

intrinsic electronic structure of the metal oxide semiconductor. Separating these contributions is particularly important for the evaluation of metal oxide electrodes for battery applications where repeated intercalation/deintercalation of working ions may alter the morphology of the electrode film.[65, 66]

CONCLUSIONS

We find that EIS data collected for solution-processed NiO and α-Fe_2O_3 films in redox-inert organic electrolyte solutions are best fit by a model circuit that comprises an RC circuit (R_1/C_1) nested inside a second RC circuit (R_2/C_2) in series with a third resistor (R_3, see circuit A in Figure 1). The magnitude of R_3 depends on the pathlength between the working and counter electrodes (Figure 7) and decreases with increasing concentration of electrolyte. We therefore interpret R_3 to be due primarily to solution resistance. The values of R_2 and C_2 depend on the size of the electrolyte ions relative to the porosity of the electrode film (Figure 6). In contrast, the value of C_1 does not depend strongly on electrolyte size or electrode morphology. Instead, the local maxima in the values of $1/C_1^2$ shift to different potentials when the underlying metal electrode is changed from Au to Pt (Figure 5). We therefore interpret R_2 and C_2 to be related to percolation of electrolyte ions through the pores of the metal oxide film to form a charge-compensating double-layer at the electrode/electrolyte interface, and R_1 and C_1 to be related to charge transfer from the underlying metal electrode into and through the metal oxide film. This work represents the first application of Circuit A to EIS data collected for inorganic thin films of metal oxide semiconductors in inert electrolyte solutions.

This work demonstrates that precluding charge transfer across the semiconductor/electrolyte interface, by performing EIS measurements in redox-inert organic electrolyte solutions, enables investigation of the impact of the semiconductor's morphology on the physical interactions between the semiconductor and electrolyte ions and provides a larger voltage window over which to characterize the electronic structure of the semiconductor itself. This information complements characterization of charge transfer across the semiconductor/electrolyte interface obtained *via* EIS measurements collected for metal oxide films in redox-active aqueous electrolytes to provide a more complete understanding of the electrochemical behavior of solution-processed metal oxide semiconductor films. The additional information obtained from EIS measurements in organic

electrolytes is particularly important for evaluating the performance of metal oxide electrodes in batteries and organic (photo)electrocatalysis.

ASSOCIATED CONTENT

Supporting Information

The supporting information contains additional characterization of the morphology, crystal structure, and composition of NiO and α-Fe_2O_3 films, simulated Bode plots for Circuit A and Circuit C illustrating the effect of varying the relative magnitudes of R_1/R_2 and C_1/C_2, representative Lissajous plots, data illustrating the impact of increasing film thickness on EIS measurements and the dependence of R_3 on the distance between the working and counter electrodes and on electrolyte concentration, plots of R_1 and R_2 versus potential for NiO films, parameters used to fit EIS data collected for metal oxide films, EIS data collected for bare Pt and Au electrodes in acetonitrile and EIS data collected for metal oxide films in an aqueous electrolyte, cyclic voltammograms of ferrocene collected using NiO and α-Fe_2O_3 films as working electrodes.

Conflicts of Interest

The authors declare no competing financial interest.

ACKNOWLEDGMENTS

This research was supported by start-up funds from the University of Rochester and by the U.S. National Science Foundation under grant number CHE-1900125. D.A.B. gratefully acknowledges support from the Department of Energy in the form of an Office of Science Graduate Student Research Award. The Rigaku Synergy-S X-ray diffraction system was purchased with funding from an NSF MRI grant (CHE-1725028). The authors thank William Brennessel from the Chemistry Department at the University of Rochester for the collection of powder X-ray diffraction data. The authors thank Christine Pratt from the Mechanical Engineering Department at the University of Rochester for her assistance acquiring powder X-ray diffraction standards data. The authors thank Nursah Kokbudak, Brian McIntyre and the URNano facilities for their technical support in X-ray photoelectron spectroscopy and transmission/scanning electron microscopy.

References

1. T. M. Gür, *Energy Environ. Sci.*, 2018, **11**, 2696-2767.
2. A. Wiebe, T. Gieshoff, S. Möhle, E. Rodrigo, M. Zirbes and S. R. Waldvogel, *Angew. Chem. Int. Ed.*, 2018, **57**, 5594-5619.
3. D. Aurbach, *J. Power Sources*, 2000, **89**, 206-218.
4. B. Klahr, S. Gimenez, F. Fabregat-Santiago, J. Bisquert and T. W. Hamann, *J. Am. Chem. Soc.*, 2012, **134**, 16693-16700.
5. B. Klahr, S. Gimenez, F. Fabregat-Santiago, T. Hamann and J. Bisquert, *J. Am. Chem. Soc.*, 2012, **134**, 4294-4302.
6. M. S. Prévot, X. A. Jeanbourquin, W. S. Bourée, F. Abdi, D. Friedrich, R. van de Krol, N. Guijarro, F. Le Formal and K. Sivula, *Chem. Mater.*, 2017, **29**, 4952-4962.
7. N. Serpone and A. V. Emeline, *J. Phys. Chem. Lett.*, 2012, **3**, 673-677.
8. K. Sivula, *J. Phys. Chem. Lett.*, 2013, **4**, 1624-1633.
9. J. Bisquert, H. Randriamahazaka and G. Garcia-Belmonte, *Electrochim. Acta.*, 2005, **51**, 627-640.
10. A. R. C. Bredar, A. L. Chown, A. R. Burton and B. H. Farnum, *ACS Appl. Energy Mater.*, 2020, **3**, 66-98.
11. M. E. Orazem and B. Tribollet, *Electrochemical Impedance Spectroscopy*, Wiley, 2017.
12. E. von Hauff, *J. Phys. Chem. C*, 2019, **123**, 11329-11346.
13. M. S. Prévot, N. Guijarro and K. Sivula, *ChemSusChem*, 2015, **8**, 1359-1367.
14. A. J. Bard and L. R. Faulkner, *Electrochemical Methods: Fundamentals and Applications, 2nd Edition*, Wiley Textbooks, 2000.
15. A. R. C. Bredar, M. D. Blanchet, R. B. Comes and B. H. Farnum, *ACS Appl. Energy Mater.*, 2019, **2**, 19-28.
16. H. Bayramoglu and A. Peksoz, *Mat. Sci. Semicon. Proc.*, 2019, **90**, 13-19.
17. R. O'Hayre, S. W. Cha, F. B. Prinz and W. Colella, *Fuel Cell Fundamentals*, Wiley, 2016.
18. G. E. Brown, V. E. Henrich, W. H. Casey, D. L. Clark, C. Eggleston, A. Felmy, D. W. Goodman, M. Grätzel, G. Maciel, M. I. McCarthy, K. H. Nealson, D. A. Sverjensky, M. F. Toney and J. M. Zachara, *Chem. Rev.*, 1999, **99**, 77-174.
19. M. Li, Z.-X. Jin, W. Zhang, Y.-H. Bai, Y.-Q. Cao, W.-M. Li, D. Wu and A.-D. Li, *Sci. Rep.*, 2019, **9**, 10438.
20. S. Boyd and V. Augustyn, *Inorg. Chem. Front.*, 2018, **5**, 999-1015.
21. L. M. Peter, in *Photocatalysis: Fundamentals and Perspectives*, eds. J. Schneider, D. Bahnemann, J. Ye, G. L. Puma and D. D. Dionysiou, The Royal Society of Chemistry, Cambridge, UK, 2016, ch. 1, pp. 1-28.
22. K.-W. Park and A. M. Kolpak, *Commun. Chem.*, 2019, **2**, 79.
23. G. M. Carroll and D. R. Gamelin, *J. Mater. Chem. A*, 2016, **4**, 2986-2994.
24. T. W. Hamann, *Dalton Trans.*, 2012, **41**, 7830-7834.
25. S. Bae, H. Kim, D. Jeon and J. Ryu, *ACS Appl. Mater. Interfaces*, 2019, **11**, 7990-7999.
26. S. Volk, N. Yazdani, E. Sanusoglu, O. Yarema, M. Yarema and V. Wood, *J. Phys. Chem. Lett.*, 2018, **9**, 1384-1392.
27. M. B. Gawande, R. K. Pandey and R. V. Jayaram, *Catal. Sci. Technol.*, 2012, **2**, 1113-1125.
28. S. Z. F. Rodzi and Y. Mohd, *2012 IEEE Symposium on Humanities, Science and Engineering Research*, 2012, DOI: DOI: 10.1109/SHUSER.2012.6268886, 531-535.
29. S. Jiao, L. Xu, K. Hu, J. Li, S. Gao and D. Xu, *J. Phys. Chem. C*, 2010, **114**, 269-273.

30. D. A. Brewster, Y. Bian and K. E. Knowles, *Chem. Mater.*, 2020, **32**, 2004-2013.
31. D. A. Brewster, D. J. Sarappa and K. E. Knowles, *Polyhedron*, 2019, **157**, 54-62.
32. V. V. Pavlishchuk and A. W. Addison, *Inorganica. Chim. Acta*, 2000, **298**, 97-102.
33. L. Wang, C.-Y. Lee and P. Schmuki, *J. Mater. Chem. A*, 2013, **1**, 212-215.
34. D. Adler and J. Feinleib, *Phys. Rev. B*, 1970, **2**, 3112-3134.
35. S.-Y. Tsai, M.-H. Hon and Y.-M. Lu, *Solid-State Electron.*, 2011, **63**, 37-41.
36. U. Ulmer, T. Dingle, P. N. Duchesne, R. H. Morris, A. Tavasoli, T. Wood and G. A. Ozin, *Nat. Commun.*, 2019, **10**, 3169.
37. Y. Xu and M. A. A. Schoonen, *Am. Mineral.*, 2000, **85**, 543-556.
38. K. Nakaoka, J. Ueyama and K. Ogura, *J. of Electroanal. Chem.*, 2004, **571**, 93-99.
39. G. Natu, P. Hasin, Z. Huang, Z. Ji, M. He and Y. Wu, *ACS Appl. Mater. Interfaces*, 2012, **4**, 5922-5929.
40. Y. Yu, K. A. Click, S.-C. Chien, J. Sun, A. Curtze, L.-C. Lin and Y. Wu, *J. Phys. Chem. C*, 2019, **123**, 8681-8687.
41. S. M. McCullough, J. M. Evans, T. Moot, A. D. Taggart, L. Troian-Gautier and J. F. Cahoon, *ACS Appl. Energy Mater.*, 2020, **3**, 1496-1505.
42. Q. Liu, L. Wei, S. Yuan, X. Ren, Y. Zhao, Z. Wang, M. Zhang, L. Shi, D. Li and A. Li, *RSC Adv.*, 2015, **5**, 71778-71784.
43. F. P. Bossu and D. W. Margerum, *Inorg. Chem.*, 1977, **16**, 1210-1214.
44. B. Klahr, S. Gimenez, F. Fabregat-Santiago, J. Bisquert and T. W. Hamann, *Energy Environ. Sci.*, 2012, **5**, 7626-7636.
45. J. Husek, A. Cirri, S. Biswas and L. R. Baker, *Chem. Sci.*, 2017, **8**, 8170-8178.
46. C. Lohaus, A. Klein and W. Jaegermann, *Nat. Commun.*, 2018, **9**, 4309.
47. W. J. Albery, G. J. O'Shea and A. L. Smith, *J. Chem. Soc., Faraday Trans.*, 1996, **92**, 4083-4085.
48. I. Herraiz-Cardona, F. Fabregat-Santiago, A. Renaud, B. Julián-López, F. Odobel, L. Cario, S. Jobic and S. Giménez, *Electrochimica Acta*, 2013, **113**, 570-574.
49. A. M. Schimpf, K. E. Knowles, G. M. Carroll and D. R. Gamelin, *Acc. Chem. Res.*, 2015, **48**, 1929-1937.
50. Y. Marcus, *J. Solution Chem.*, 2008, **37**, 1071.
51. A. L. Rohl and D. M. P. Mingos, *Dalton Trans.*, 1992, 3541-3552.
52. N. Elgrishi, K. J. Rountree, B. D. McCarthy, E. S. Rountree, T. T. Eisenhart and J. L. Dempsey, *J. Chem. Ed.*, 2018, **95**, 197-206.
53. Parveen and R. Kant, *Electrochim. Acta.*, 2013, **111**, 223-233.
54. N. Tanibata, R. Morimoto, K. Nishikawa, H. Takeda and M. Nakayama, *Anal. Chem.*, 2020, **92**, 3499-3502.
55. K. Xu and A. von Wald Cresce, *J. Mater. Res.*, 2012, **27**, 2327-2341.
56. R. Kant and M. B. Singh, *Phys. Rev. E*, 2013, **88**, 052303.
57. J. Chmiola, C. Largeot, P.-L. Taberna, P. Simon and Y. Gogotsi, *Angew. Chem. Int. Ed.*, 2008, **47**, 3392-3395.
58. M. O'Donoghue, R. Garrett, V. Datta, P. Roberts and T. Aben, *Mater. Performance*, 2003, **42**, 36-41.
59. K. Shimizu, A. Lasia and J.-F. Boily, *Langmuir*, 2012, **28**, 7914-7920.
60. M. B. Stevens, L. J. Enman, A. S. Batchellor, M. R. Cosby, A. E. Vise, C. D. M. Trang and S. W. Boettcher, *Chem. Mater.*, 2017, **29**, 120-140.

61. Q. Huang, Q. Luo, Z. Chen, L. Yao, P. Fu and Z. Lin, *Environ. Sci. Water Res. Technol.*, 2018, **4**, 1145-1151.
62. O. Mizrahi, N. Amir, E. Pollak, O. Chusid, V. Marks, H. Gottlieb, L. Larush, E. Zinigrad and D. Aurbach, *J. Electrochem. Soc.*, 2008, **155**, A103.
63. J. Xie, A. D. Sendek, E. D. Cubuk, X. Zhang, Z. Lu, Y. Gong, T. Wu, F. Shi, W. Liu, E. J. Reed and Y. Cui, *ACS Nano*, 2017, **11**, 7019-7027.
64. L. Xia, L. Yu, D. Hu and G. Z. Chen, *Mater. Chem. Front.*, 2017, **1**, 584-618.
65. J. Y. Xiang, J. P. Tu, Y. Q. Qiao, X. L. Wang, J. Zhong, D. Zhang and C. D. Gu, *J. Phys. Chem. C*, 2011, **115**, 2505-2513.
66. Q.-C. Zhuang, T. Wei, L.-L. Du, Y.-L. Cui, L. Fang and S.-G. Sun, *J. Phys. Chem. C*, 2010, **114**, 8614-8621.